The messy death of a multiple star system and the resulting planetary nebula as observed by JWST

De Marco, O.; Akashi, M.; Akras, S.; Alcolea, J.; Aleman, I.; Amram, P.; ... ; Zijlstra, A.A.

nature astronomy

Article

https://doi.org/10.1038/s41550-022-01845-2

The messy death of a multiple star system and the resulting planetary nebula as observed by JWST

Received: 2 September 2022

Accepted: 26 October 2022

Published online: 8 December 2022

Check for updates

A list of authors and their affiliations appears at the end of the paper

Planetary nebulae—the ejected envelopes of red giant stars—provide us with a history of the last, mass-losing phases of 90% of stars initially more massive than the Sun. Here we analyse images of the planetary nebula NGC 3132 from the James Webb Space Telescope (JWST) Early Release Observations. A structured, extended hydrogen halo surrounding an ionized central bubble is imprinted with spiral structures, probably shaped by a low-mass companion orbiting the central star at about 40–60 au. The images also reveal a mid-infrared excess at the central star, interpreted as a dusty disk, which is indicative of an interaction with another closer companion. Including the previously known A-type visual companion, the progenitor of the NGC 3132 planetary nebula must have been at least a stellar quartet. The JWST images allow us to generate a model of the illumination, ionization and hydrodynamics of the molecular halo, demonstrating the power of JWST to investigate complex stellar outflows. Furthermore, new measurements of the A-type visual companion allow us to derive the value for the mass of the progenitor of a central star with excellent precision: $2.86 \pm 0.06\ M_{\odot}$. These results serve as pathfinders for future JWST observations of planetary nebulae, providing unique insight into fundamental astrophysical processes including colliding winds and binary star interactions, with implications for supernovae and gravitational-wave systems.

Planetary nebulae (PNe) are the ejected envelopes of intermediate-mass (~1–8 $M_{\odot}$) stars that have recently terminated their asymptotic giant branch (AGB) stage of evolution. Moving outwards from the hot pre-white dwarf star (temperature, $T \approx 10^5$ K) that is the progeny of the AGB star, the structure of a canonical quasi-spherical PN consists of a hot, sparse, wind-heated bubble ($T \approx 10^7$ K) surrounded by a dense shell of displaced, ionized AGB gas ($T \approx 10^4$ K), which in turn may still be surrounded by 'pristine', cold ($T \approx 10^2$ K), molecule- and dust-rich AGB ejecta. However, if the progenitor star interacted with a companion(s) during its post-main-sequence evolution, we would expect departures from spherical symmetry, perhaps including spiral structures and arcs (for example, refs. [1–3]), the presence of a dense, molecule-rich torus (for example, ref. [4]), one or more pairs of polar lobes formed by fast, collimated outflows and jets (for example, refs. [5,6]) and/or a dusty, circumbinary disk[7]. The type of interaction depends on the orbital radius, and ranges from common envelope evolution for close binaries[8], to accretion disks and gravitational focusing of the wind for wider systems[9–11], to displacement of the central star from the geometric centre of the nebula for the widest systems[12].

The first Hubble Space Telescope (HST) images of PNe revealed a breathtaking new world of details and far more complex structures than had been gleaned from ground-based images (for example, refs. [13,14]). The superb spatial resolution of HST, combined with high-resolution, kinematic mapping, enabled the construction of detailed three-dimensional

e-mail: orsola.demarco@mq.edu.au

https://doi.org/10.1038/s41550-022-01845-2

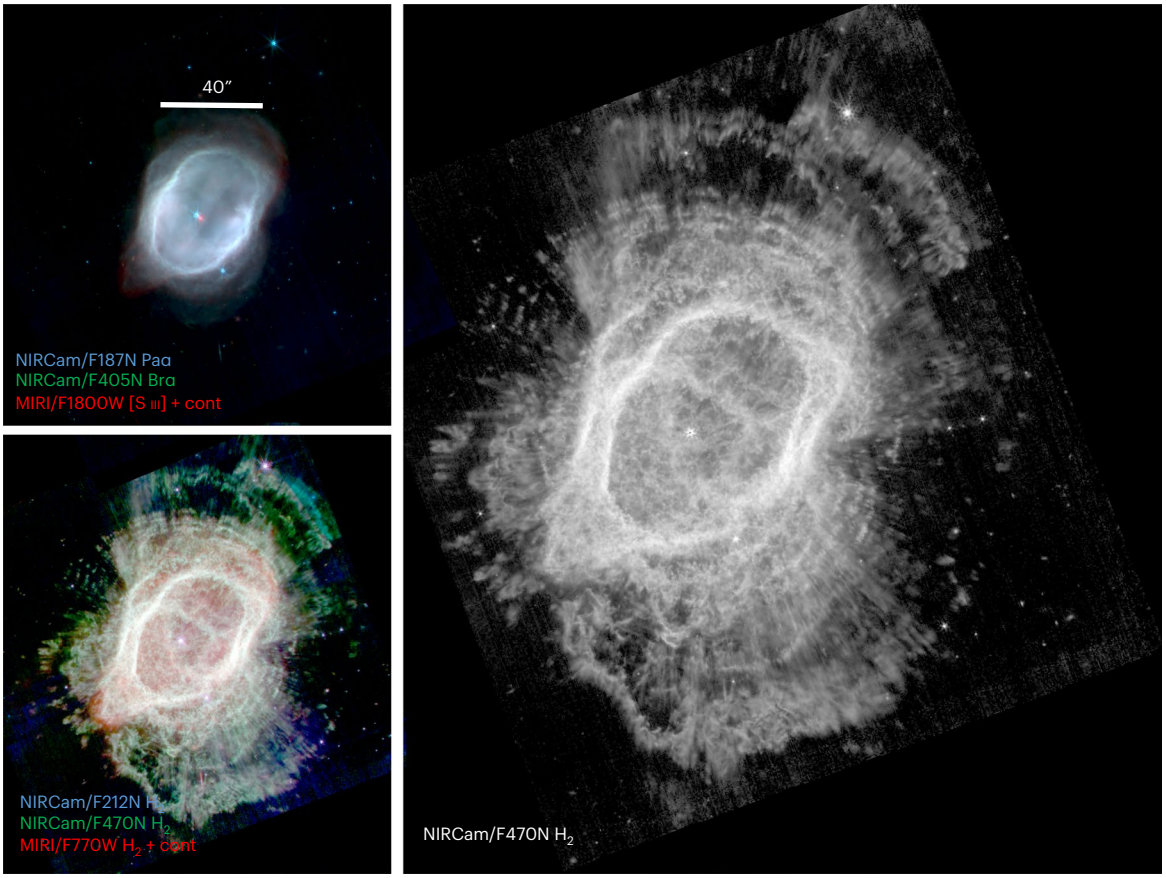

Fig. 1 | JWST images of the PN NGC 3132. Left: colour overlays of JWST NIRCam and MIRI images that cleanly distinguish between the PN's ionized gas (that is, H II region; top) and molecular gas (as seen in H_2; bottom). cont., continuum emission. Note the sharp contrast between the relatively smooth appearance of the H II region and the flocculent structure of the H_2 ring system and extended H_2 halo. These images are presented with square-root and log intensity stretches, respectively, from the background sky to peak intensity levels in each image. Right: a greyscale, single filter (F470N), zoomed-in NIRCam image that more readily shows details of the flocculent H_2 halo. North is towards the top and east is towards the left.

(3D), morpho-kinematic models, which, together with hydrodynamic models (for example, refs. [15,16]), started to connect our understanding of the evolution of the structures and kinematics of PNe with their possible binary star origins (for example, refs. [17–19]).

The James Webb Space Telescope (JWST), with its superb sensitivity and high spatial resolution from near- to mid-infrared (IR), is now poised to enable a leap of similar magnitude in our understanding of PNe. This journey began when JWST released near- and mid-IR images of just one PN, NGC 3132, as part of its Early Release Observations (ERO) programme. NGC 3132 is a nearby (at a distance of 750 pc), molecule-rich[20,21], ring-like PN, long known to harbour a visual binary comprising the central (progenitor) star and an A-star companion. In this Article, we show that the JWST ERO images contain multiple, new lines of evidence that NGC 3132 is the recent product of a hierarchical multiple progenitor stellar system, which has experienced both indirect and direct interactions involving one or more components. Such binary interactions have taken on new importance in the era of gravitational-wave detectors (Laser Interferometer Gravitational-wave Observatory[22] and Laser Interferometer Space Antenna[23]) and ambitious transient surveys[24]. Indeed, PNe such as NGC 3132 offer unique insight into the formation pathways of the close, single- and double-degenerate binaries that are eventual gravitational-wave sources and (perhaps) type Ia supernova progenitors[25–27].

Results

A flocculent molecular halo surrounding an ionized bubble. Figure 1 shows colour overlays of Near-IR Camera (NIRCam) and Mid-IR Instrument (MIRI) images of NGC 3132 that highlight JWST's clean separation of the PN's ionized (H II) and molecular (H_2) regions. The full resulting JWST image suite, along with basic information, is presented in 'Specification of JWST NIRCam and MIRI imaging' in Supplementary Information and Supplementary Fig. 1. The images reveal the extent and detailed structure of the halo of molecular gas that lies exterior to the nebula's central, ionized cavity, and its bright and thin, peripheral elliptical ring (compare ref. [28]). This molecular halo is well detected in rovibrational H_2 emission at 2.12 μm (1–0 S(1)), 4.7 μm (0–0 S(9)) and 7.7 μm (0–0 S(5)) out to 60 arcsec (~0.22 pc at the adopted distance of 754 pc; see 'Properties and distance of NGC 3132' in Methods) from the central star. Spatially organized structures—arcs and patterns of spikes emanating radially outwards—are observed in the halo H_2 emission on medium to large scales, while molecular arcs, loops and knots are detected on size scales from ~500 au down to the limiting (~75 au) resolution of the images. The typical thickness of the bright H_2 rings that surround the nebular core is ~1–2 arcsec (~750–1,500 au), measured at 2.1 μm, 4.7 μm and 7.7 μm.

Figure 1 conclusively demonstrates that the molecular gas is much clumpier than the ionized gas component of NGC 3132 (Supplementary Fig. 3). In H_2 recombination lines and [S III] emission (Fig. 1, top left), the nebula's central ionized cavity (within ~25 arcsec of the central star) appears as a relatively smooth elliptical region that is bounded by a single, sharped-edged ring; whereas in H_2 (Fig. 1, bottom left), this same central region appears as a far more complex system of clumpy filaments. The regions in and around this bright, inner H_2 ring system contain as many as 20 dense clumps (knots) per square arcsec, implying the total number of H_2 knots in this region exceeds 10^4. The H_2 knots in the outer (halo) region are less distinct and farther apart.

https://doi.org/10.1038/s41550-022-01845-2

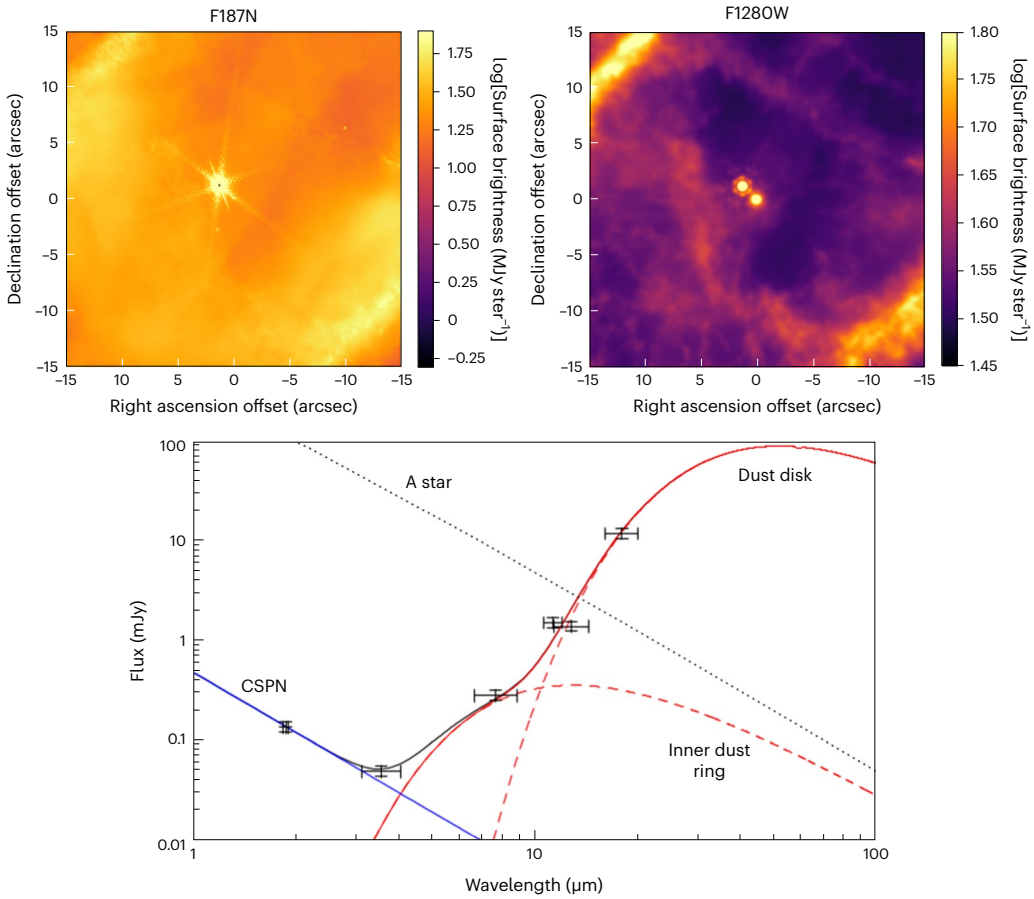

Fig. 2 | The dusty central star of the PN NGC 3132. Top: JWST NIRCam F187N (left) and MIRI F1280W (right) images of the central region of NGC 3132. The JWST MIRI images reveal the detection of a mid-IR excess at the nebula's true (hot, compact) central star, which is seen projected ~1.7″ (~1,300 au) southwest of the main-sequence A-type companion (which is far brighter shortwards of ~10 μm). North is up and east is to the left. Bottom: the near-IR to mid-IR spectral energy distribution of the central star of the PN (CSPN) of NGC 3132 overlaid with a model consisting of a combination of a hot blackbody spectrum representing the central star's photosphere (blue line) and a dusty circumstellar double disk model to fit the near- and mid-IR data points (red line, with the individual disks as dashed lines). The wide companion, A star's spectral energy distribution is shown as a dotted line. Vertical error bars are set at 10% of the flux values, while horizontal bars show the width of the bandpass.

The presence of radially directed spike features in the H_2 halo indicates that direct irradiation by ultraviolet photons, leaking through less dense gas between the inner ring system's H_2 knots, are most likely responsible for the excitation of the IR H_2 lines in the extended halo, although shock excitation cannot be completely ruled out (see ref. [29] and references therein). The relative lack of H_2 halo emission to the east–northeast and west–southwest of the central star then indicates a general lack of central star ultraviolet illumination, as opposed to a lack of halo molecular mass in those directions (see 'Discussion'). Measurements of the extinction of background nebulosity through representative knots suggests typical knot densities of ~10^6 cm^{-3} and masses of ~10^{-5} $M_\odot$ (see 'Densities, masses and excitation of the H_2 knots' in Methods), suggesting a total H_2 mass of ~0.1 $M_\odot$ in the central ring region.

The system of (broken) concentric arcs revealed in the H_2 halo by the JWST images is similar to those observed in the extended, dusty envelopes of many AGB stars, proto-PNe and PNe (for example, refs. [1,32–35]). A widely accepted scenario to explain the formation of such arc systems is the modulation of an AGB wind by a stellar or substellar companion, creating 3D spiral-like patterns along the orbital plane (see refs. [1,32–35] and references therein). The average angular distance between the arc structures, 2 arcsec, implies an orbital period of 290–480 yr and an orbital separation of 40–60 au between the central star and the companion that shapes the mass loss. Here we have assumed a companion mass of 0.2 $M_\odot$, the highest-mass main-sequence star that could hide in the present-day central star's glare yet still form a visible arc system (other parameters are an expansion velocity in the range 15–25 km s^{-1} (ref. [31]) and an assumed late-AGB central star mass of ~0.8 $M_\odot$; probably still 0.1–0.2 $M_\odot$ larger than the post-AGB mass). The bright A2V visual companion seen at ~1,300 au projected separation from the central star cannot be responsible, suggesting (at least) a triple system in a stable configuration.

The dusty central star. In the MIRI images obtained at wavelengths longer than 10 μm, the faint central star appears as bright or brighter than its A2V main-sequence visual companion[36] (Fig. 2). This IR excess was undetectable in the mid-IR at lower spatial resolution (for example, in Wide-field Infrared Survey Explorer images[37]) because of the surrounding bright nebulosity. The JWST-discovered IR excess indicates that a considerable amount of warm dust is present around the ultrahot (~110 kK) PN central star. The thermal IR source appears marginally extended in the 11.3 μm and 12.8 μm MIRI images with an apparent size of ~300 au (full-width at half-maximum (FWHM)) at 12.8 μm (see 'PSF measurements of the central star' in Methods).

The bottom panel of Fig. 2 shows the central star's near- to mid-IR spectral energy distribution fitted by a combination of a hot stellar photosphere represented by a blackbody curve and two curves to fit the IR data points. The two curves are generated with a model that follows

https://doi.org/10.1038/s41550-022-01845-2

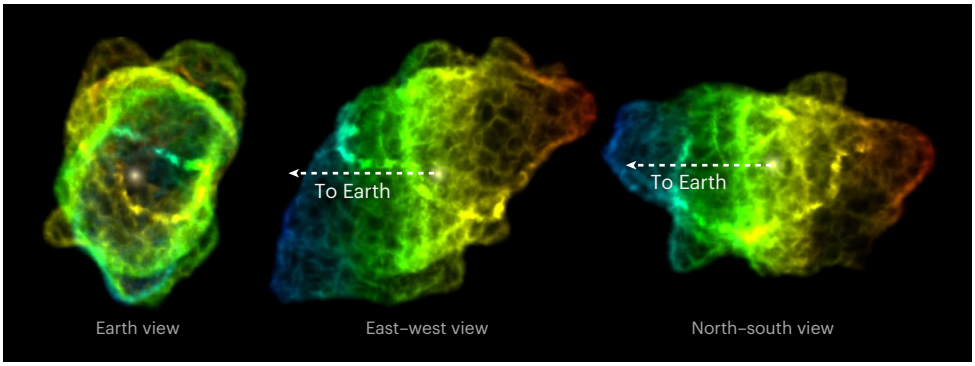

Fig. 3 | Morpho-kinematic reconstruction of the ionized cavity of PN NGC 3132. Emission in the [N II] line as seen from Earth (left; north is towards the top and east is towards the left), a view from the east, which we call the east–west view (middle), and a view from the north, which we call the north–south view (right). The colour coding is for Doppler shift as seen from Earth, with blue for material approaching the observer, red for receding gas and green for no velocity along the observer's line of sight. We note the prominent green (zero Doppler shift) belt in the middle image, and the filament that wraps around the waist of the ellipsoid and that is red-shifted on one side and blue-shifted on the other. A fly-through video of this model can be found as Supplementary Video 1 and also at this link.

closely that of ref. [38] for the Helix nebula. A number of 100 μm grains are taken as blackbody spheres with temperatures set by absorption and re-emittance of the stellar luminosity (200 $L_{\odot}$; a correction factor is then applied to simulate a grain size distribution between 60 μm and 1,000 μm, as done by ref. [38]). The temperature varies as $d^{0.5}$, where d is the distance to the star. The surface density of the disk is taken as constant. The resulting blackbody radiation is calculated at each radius, and the emission is summed over all radii. A better model will require radiative transfer, actual dust emissivities, a range of grains sizes, and for the silicate feature, the inclination of the disk. This will be explored in a future paper.

The best-fit model disk has an inner radius of 55 au, an outer radius of 140 au, and a dust mass of 3×10^{26} g or 2×10^{-7} $M_{\odot}$ (approximately 0.05 Earth masses). The dust temperature range (inner to outer radius) is 130 K to 80 K. The outer radius of 140 au, although poorly constrained, is consistent with the deconvolved half-width of the marginally extended mid-IR source. These dimensions resemble those inferred for the disk orbiting the central star of the Helix nebula (35–150 au; ref. [38]), but the dust mass is somewhat smaller (compare 0.13 Earth masses). The outer radius could be slightly larger, if the 18 μm flux is underestimated because of detector saturation. An additional inner, hotter disk—with a radius between 3 au and 8 au, a temperature between 550 K and 335 K (inside to outside), and a very small mass of 2×10^{22} g (approximately 0.02 times the mass of Ceres)—is needed to fit the 3.5 μm and 7 μm fluxes. Although this model does not constrain the geometry of the distribution to be that of a disk, the reasoning behind a disk structure is based on a physical reasoning whereby only a rotating Keplerian disk can be shown to be stable and relatively long-lived, whereas other structures, such as shells, are easily shown to be unstable[39].

The A2V companion is slightly evolved[36] and has a mass of $M_{\rm A2V} = 2.40 \pm 0.15\ M_{\odot}$, using the stellar structure model PARSEC isochrones (see 'Central star system's masses' in Methods). Its visual companion, the PN central star, must have descended from a more massive star, as it has evolved faster. Extrapolating the same PARSEC isochrone gives an initial main-sequence mass for the central star of $M_{\rm i} = 2.86 \pm 0.06\ M_{\odot}$. This is potentially the most precise initial mass for any PN central star or white dwarf yet determined.

We estimate the error to be 0.16 $M_{\odot}$ if we add systematic effects between different isochrone models (see 'Central star system's masses' in Methods).

The current (near final) mass of a PN central star descended from such an ~2.9 $M_{\odot}$ progenitor is predicted to be $M_{\rm f} \approx 0.66 \pm 0.05\ M_{\odot}$ based on initial–final mass relations[40], albeit with larger systematic uncertainties that are dependent on details of the mass-loss process adopted by the models. It is noteworthy that photoionization models of the nebula require a cooler, dimmer and overall less massive central star ($0.58 \pm 0.03\ M_{\odot}$) than what we have found.

We find that we can reconcile the mass of the star today and that of the photoionization model, while also matching the nebular abundances and the nebular age, if we assume that the AGB evolution of a 2.86 $M_{\odot}$ star, was interrupted by a binary interaction that ejected the envelope. We conjecture that the AGB evolution was interrupted at a core mass of 0.61 $M_{\odot}$, because for larger values, the C/O ratio of the stellar envelope gas would increase above unity (counter to the observation of crystalline silicate grains). At larger masses, the N/O ratio would also increase above the observed value of 0.42.

Discussion

The first striking discovery of JWST is the presence of the dusty disk around the ultrahot central star. This indicates that JWST can accurately detect dusty disks lighter than Ceres, as far as ~700 pc away. For our PN, the presence of such a disk orbiting the PN central star favours a close binary interaction, where the companion either merged with the primary star, or is still in orbit but is undetected (mass <0.2 $M_{\odot}$; based on an unresolved or barely resolved, equal-brightness companion); in either case, the companion has donated a substantial fraction of its angular momentum to the gas[41,42]. Observationally, such disks around PN central stars, although rare, appear to be by and large associated with known or strongly suspected binarity[39] and may be related to circumbinary disks detected around other classes of post-AGB binary stars[43].

An interacting binary scenario is reinforced by the shape of the ionized cavity, which represents the inner, most recent, mass-loss phase, when the already hot central star emitted a fast, tenuous wind. Pairing the JWST images with spatially resolved spectroscopy, we constructed a 3D visualization of this cavity (see 'Morpho-kinematic modelling' in Supplementary Information). In Fig. 3, we show that this inner cavity is inferred to be an expanding prolate ellipsoid with its long axis tilted at approximately 30° to the line of sight. Its surface is not smooth and presents instead a number of protuberances, most of which can be paired via axes passing through, or very near the central star. Prolate cavities such as these, with misaligned structures, are common in PN and are probably sculpted by jets from interacting binaries in the earlier, pre-PN phase of the nebula[44], with additional details added during the interaction between the AGB wind and post-AGB fast wind and via the process of PN ionization.

The numerous protuberances clearly evident in the 3D reconstruction could arise from ionized gas breaking out of the inner cavity through an uneven outer shell. The apparent pairing between these

https://doi.org/10.1038/s41550-022-01845-2

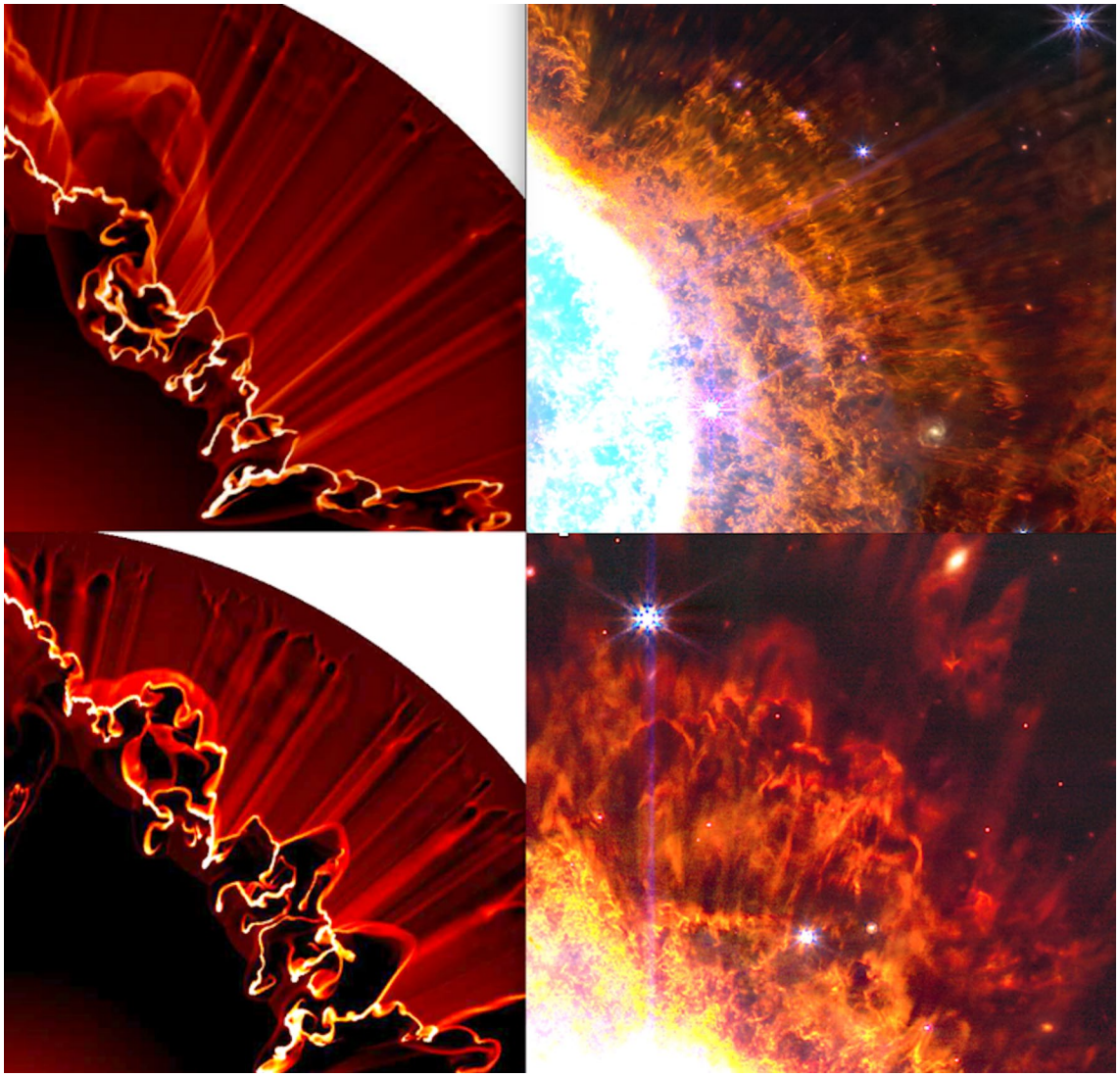

Fig. 4 | The physical interpretation of the flocculent H_2 structure. Left: a hydrodynamic simulation showing the formation of nebular structures external to the main ionized region, compared with two quadrants of the JWST images of NGC 3132 (right). Top: the simulation snapshot at 3,800 yr from the on-set of ionization is compared with similar straight spikes in one region of the nebula (top right image, north is to the top-left and east is towards the bottom-left). Bottom: at 4,000 yr, the spikes thicken and bend as is also seen in a different part of the nebula (north to the right and east to the top). This demonstrates temporal evolution in different parts of the nebula.

protuberances may argue instead for the presence of intermittent and toppling jets[45]. To generate jets over such a wide range of axes, an interacting binary is not enough, and one would have to conjecture that the central star is or was a member of not just a close binary, but of an interacting triple system[46]. Recent studies of interactions in triple systems[47,48] also argue for the possibility of interactions yielding complex ejecta.

Outside the ionized ellipsoid, one encounters material ejected earlier in the star's history. The AGB mass loss, at rates of up to ~10^{-5} $M_{\odot}$ yr^{-1} and speeds of ~10 km s^{-1} over an ~10^5 yr timescale[49], generates an enormous, expanding envelope of molecular gas and dust. The H_2 halo imaged by JWST constitutes the most recently ejected (inner) region of this AGB envelope. The spikes observed in the halo (Fig. 1, right) show that the inner cavity is very porous, although less so near the minor axis where the cavity edges are brightest, densest and least fractured.

The JWST images motivated 2D hydrodynamic simulations to replicate these flocculent structures. In Fig. 4, we see two time snapshots towards the end of a simulation where an inner, faster wind from the heating central star and its ionizing radiation, plough into the dense AGB (halo) material (see 'Hydrodynamic modelling' in Methods). The fragmentation that happens at the interface of the swept-up material also creates the variable opacity needed to shield some of the wind material from ionizing radiation, which then quickly recombines and allows the formation of molecules. Non-ionizing radiation leaks more readily because the opacity above 913 Å is lower. These photons produce fluorescence of H_2.

In Fig. 4, we see two time snapshots towards the end of the simulation. In the top left image, we see a set of approximately radial spikes, but 200 yr later, those straight and thin spikes evolve to thicker and sometimes curved ones. In the right images of Fig. 4, two different parts of the nebula exhibit thinner and straighter spikes (top right) or thicker, bent ones (bottom right). Although the entire nebula was ejected and ionized over a short time interval, there can be a delay in the evolution of a given spike in a specific part of the nebula, related to the local opacity in the swept-up shell. Figure 4 suggests that differences of only ~200 yr in the timescales of mass ejection and/or the progress of illumination along specific directions can explain the marked differences observed in the flocculent structure around the nebula.

https://doi.org/10.1038/s41550-022-01845-2

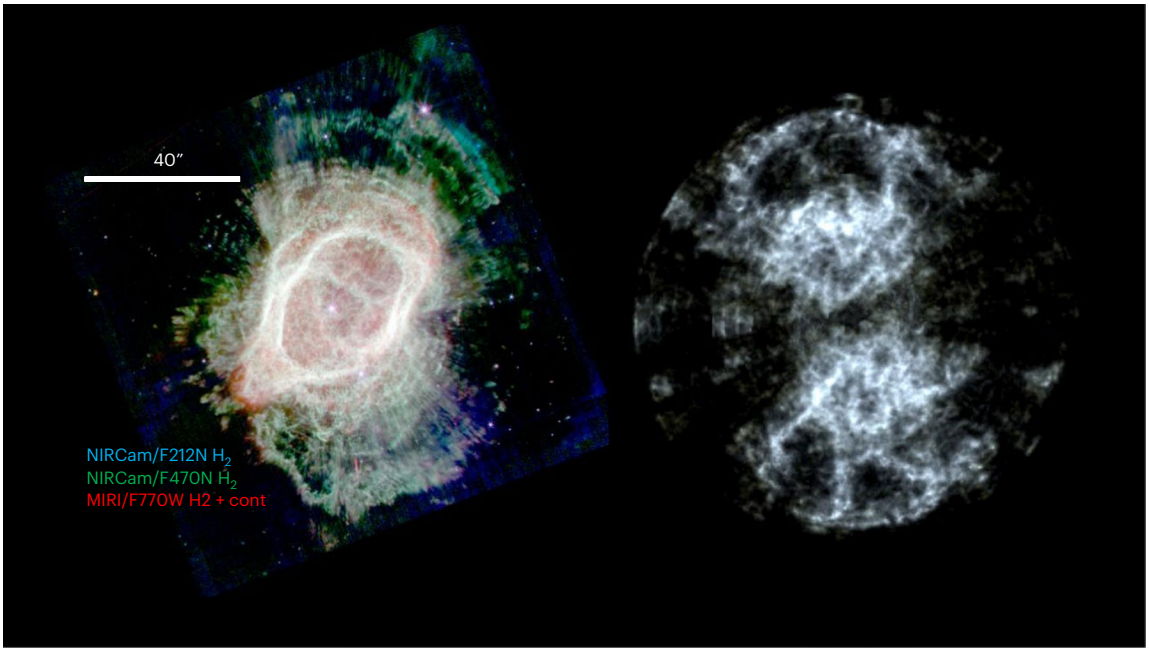

Fig. 5 | Approximate illumination model of the H_2 halo of PN NGC 3132. Left: the JWST colour composite image showing the H_2 extended structure. Right: the projected Shape image after assuming two concentric, thick, uninterrupted shells of material, illuminated by the central star, through a porous ellipsoid with reduced opacity in the polar regions. A fly-through video of this model can be found as Supplementary Video 2 and also at this link.

The successful modelling of illumination percolating unevenly into the molecular halo (Fig. 4) motivated a further geometric model of the halo, presented in Fig. 5. Figure 5 compares the extended H_2 structures as imaged by JWST with a model consisting of two thick, concentric, unbroken but clumpy, shells of material that are illuminated by the central star through a porous ellipsoid representing the boundary of the ionized cavity, with reduced opacity in the polar regions. As a result of the uneven illumination, the distribution of H_2 material appears fragmented and is generally brighter towards the polar regions (and suppressed along the equatorial plane) of the central ellipsoidal, ionized region. The distribution seen in the JWST H_2 images could be reproduced more closely by altering the opacity of the inner ellipsoid. Fly-though videos of the 3D reconstructions of both the inner ellipsoid (Fig. 3) and the outer H_2 halo (Fig. 5) can be found following the links in the captions.

The arches in the JWST images are not smeared as is typical of those seen in projections (for example, ref. [50]), but are instead sharp. This possibly indicates that these arches are on or near the plane of the sky, indicating that the orbit of the companion at ~40–60 au is closely aligned to the waist of the inner ellipsoid. This companion cannot partake in the formation of the disk around the central star, although it may play a secondary role in the shaping of other PN structures. It is also unlikely to have launched strong jets, because at such distance from the central star the accretion rate would be very low. As such, this would be an additional companion to the inner binary (or triple), making it a tertiary (or quaternary) companion.

The visual A-type companion would then be a fourth (fifth) member of the group, an almost complete bystander from the point of view of interaction and shaping, but critically important for this study. Its well-measured mass, and slight evolved status, constrained the initial mass of the central star: $(2.86 \pm 0.06)\ M_{\odot}$.

To reconstruct the events that lead to the demise of the progenitor of NGC 3132, the PN acts like a murder scene. The A-type companion could not have partaken in the interaction that unravelled the AGB star, but was (and is) certainly present. A second companion at 40–60 au left an indelible trail of its presence in the form of arcs, but was not close enough to generate the dusty disk, nor shape the ionized cavity, implying that there must have been at least another accomplice. This points the finger at a close-by companion that is either avoiding detection or has perished in the interaction (merged). If the numerous protuberances seen in the ionized cavity come in pairs, then tumbling jet axes would be needed and this would point the finger to the presence of a second, close companion[47,48], which would make the system a quintet. Even ignoring the putative second, close companion, we can state with good degree of certainty that the system is at least a quartet. Systems of four or five stars orbiting within a few ×1,000 au are not impossibly rare for primary stars in the progenitor mass range of interest here (for example, HD 104237; ref. [51]); indeed, present estimates indicate that 50% or more of stars of 2–3 $M_{\odot}$ are in multiple systems, and of order 2% of A-type stars have four companions[52].

JWST is at the starting gate of its promise as an astrophysical pathfinder. With complementary radio, interferometric and time-resolved observations, it can find the temporal signatures of active convective mass ejection from the surfaces of AGB stars and the subsequent gravitational influence of companion stars in dynamically and thermally complex outflows. Thus, JWST offers the potential to intimately connect the histories of PNe and the role of close stellar companions to studies of chemical evolution, nebular shaping and binary interactions for the next century.

Methods

Properties and distance of NGC 3132

The inner, ionized cavity of NGC 3132 is elliptical in shape, with a major axis of ~40 arcsec (0.15 pc) and an electron density of $n \approx 10^3$ cm^{-3}. The ionization structure and abundances were the subject of a recent study by ref. [53]. The nebula is also known to be molecule rich[20]; it is among the brightest PNe in near-IR H_2 emission[21,54].

A bright A2V star is found near the centre of the PN, but is too cool to be the ionizing star; the actual PN progenitor is much fainter and is located ~1.7 arcsec to the southwest of the A star[55,56]. The A2V star has the same radial velocity and extinction as the PN, and its proper motion ($\mu_\alpha = -7.747$ mas yr^{-1}, $\sigma_{\mu_\alpha} = 0.026$; and $\mu_\delta = -0.125$ mas yr^{-1}, $\sigma_{\mu_\delta} = 0.031$, where μ_α and μ_δ are the proper motions in declination and right ascension, respectively, while $\sigma_{\mu\alpha}$ and $\sigma_{\mu\delta}$ are their respective errors) agrees

with that of the central star ($\mu_\alpha = -7.677$ mas yr^{-1}, $\sigma_{\mu_\alpha} = 0.235$; and $\mu_\delta = 0.197$ mas yr^{-1}, $\sigma_{\mu_\delta} = 0.275$), demonstrating that the PN progenitor and A-type companion constitute a comoving visual binary. The distance to NGC 3132 is obtained from Gaia Data Release 3 (DR3) measurements of this visual binary. No Gaia DR3 radial velocity is available for the optically faint central star (the PN progenitor). However, the brighter (A type) visual companion and the PN have the same radial velocity: (-11.4 ± 1.6) km s^{-1} for the A star from Gaia, and (-10 ± 3) km s^{-1} for the PN from ref. [57]. The A star and PN central star also have compatible Gaia DR3 proper motions (within 1.5σ).

The brighter, A-type star has a Gaia DR3 geometric distance (median of geometric distance posterior) of 754 pc, with lower and upper 1σ-like confidence intervals (16th and 87th percentiles of the posterior) of 18 pc and 15 pc, respectively[58]. The fainter central star has a Gaia DR3 geometric distance of 2,124.7 pc, with lower and upper 1σ-like bars of 559.1 pc and 1,464.5 pc, respectively. The quality flags of the astrometric solution for this star are not optimal, most likely due to the vicinity of the much brighter A star; in particular, the goodness of fit along the scan is 16.9, but it should be close to unity. We therefore adopt the Gaia DR3 distance to the central star's visual A-type companion, 754^{+15}_{-18} pc, as the distance to the PN.

Densities, masses and excitation of the H_2 knots

The clumpiness of NGC 3132 in H_2 emission links this nebula to other molecule-rich PNe, such as the Helix nebula (NGC 7293 (refs. [59–62])), the Ring nebula (NGC 6720 (ref. [63])) and the hourglass-shaped (bipolar) nebula NGC 2346 (ref. [64]), in which the molecular emission seems to be associated with dense knots that are embedded in or surround the ionized gas. The origin of such H_2 knots in PNe—as overdensities in the former AGB wind, versus formation in situ following recombination of H, as the central star enters the cooling track—remains an open question[65]. In contrast to the Helix nebula, there is little evidence for cometary tails emanating from the knots in the inner regions of NGC 3132. However, the NGC 3132 system of approximately radially directed H_2 spikes external to the main H_2-bright ring system has close analogues in, for example, the Ring and Dumbbell nebulae[21,63].

Some H_2 knots in NGC 3132 are seen in absorption against the bright background nebular emission. This extinction is apparent not only in optical (HST) images but also, surprisingly, in the JWST NIRCam near-IR images (Supplementary Fig. 4). We measured the extinction at 1.87 μm for two knots seen in absorption against the (Paschen α (Paα)) nebula background: the largest knot on the west side (coordinates 10:07:00.4, −40:26:08.8), and one of the darkest on the east side (10:07:02.5, −40:26:00.3). The diameters of these knots are ~0.36 arcsec and ~0.15 arcsec, and their extinction is ~0.57 mag and ~0.25 mag (at 1.87 μm), respectively; using the dust extinction law $A(\lambda)/A(V)$ (using the ratio of extinction, A, at a selected wavelength, λ, to the extinction, A, in the V band) from ref. [66], the corresponding values of $A(V)$ are 3.9 mag and 1.7 mag assuming $R_V = 3.1$. We then estimate the hydrogen column densities N(H) from these extinction measurements, and convert to the hydrogen density n(H) of the knot by assuming that the knot diameters are roughly equivalent to their depths along the line of sight. Using the conversion between $A(V)$ and N(H) from ref. [67], where H is the combination of H^0, H^+ and H_2, the estimated column densities are $N(\mathrm{H}) = 7.3 \times 10^{21}$ cm^{-2} and $N(\mathrm{H}) = 3.2 \times 10^{21}$ cm^{-2}, respectively. For the adopted distance of 754 pc, the estimated densities are $n(\mathrm{H}) \approx 2 \times 10^6$ cm^{-3} for both knots. These densities suggest knot masses of $10^{-5}\,M_\odot$, similar to the typical knot ('globule') masses found in the Helix nebula[68].

The critical density of excitation of the 2.12 μm H_2 1–0 S(1) line at a kinetic temperature of 2,000 K is 9×10^5 cm^{-3} (ref. [69]), if the collision partner is H. The critical density is higher for the 1–0 S(1) line than for the 0–0 S(9) 4.69 μm H_2 line (6×10^4 cm^{-3}; refs. [69,70]). Hence, the excitation of H_2 should be nearly thermal if the gas temperature is sufficiently high, with the caveat that both critical densities are higher if the primary collision partner is H_2 rather than H.

PSF measurements of the central star

To ascertain whether the mid-IR source associated with the PN central star is extended, we measured the JWST instrumental PSF, using Gaussian fitting of field stars. We measured Gaussian FWHMs of 0.29 arcsec, 0.40 arcsec, 0.44 arcsec and 0.58 arcsec at 7.7 μm, 11.3 μm, 12.8 μm and 18 μm, respectively. We also measured two compact, slightly resolved galaxies in the field.

We then repeated the procedure for the central star. No fit was possible at 18 μm, due to saturation (Supplementary Fig. 5). At 7.7 μm, the central star is on the edge of the diffraction spike of the A star, and only an upper limit on the FWHM could be obtained. However, measurements of the PN central star image in the 11.3 μm and 12.8 μm filters gave consistent results, with measured FWHMs of 0.55 arcsec and 0.60 arcsec, significantly larger than the respective PSFs and comparable to the two field galaxies. Gaussian deconvolution using the PSF yields deconvolved FWHM values for the central star of ≤0.3 (≤230 au) at 7 μm, and 0.4 arcsec (300 au) at 11.3 μm and 12.8 μm. The extent of the central star at 18 μm is ≥0.9 arcsec in diameter (Supplementary Figs. 5 and 7).

Central star system's masses

We determined the mass of the A-star companion using version 1.2 of the PARSEC isochrones[71] for solar metallicity, taken as $Z = 0.0152$. We used a bolometric magnitude $M_{\mathrm{bol},0} = (0.34 \pm 0.25)$ mag and the GAIA DR3 spectroscopic temperature $T_{\mathrm{eff}} = (9{,}200 \pm 200)$ K, where the errors are conservative. The star is confirmed to be beginning to turn off the main sequence, in a phase where the luminosity of $(57 \pm 15)\,L_\odot$ increases by 0.1% per million years and the temperature decreases by 7 K per million years (Supplementary Fig. 6). The isochrones yield an age of $(5.3 \pm 0.3) \times 10^8$ yr and a mass of $M_{\mathrm{A2V}} = (2.40 \pm 0.15)\,M_\odot$. The central star of the PN is evolving on the same isochrone, but from a more massive star as it has evolved further. We use the same isochrones to determine the initial mass of a star on the thermal-pulsing AGB, the phase where the central star ejected the envelope. This gives an initial mass for the central star of $M_{\mathrm{i}} = (2.86 \pm 0.06)\,M_\odot$. We have carried out the same isochrone fitting using an alternative stellar evolutionary model (the Dartmouth code[72]). Both the A2V star mass and the mass of the progenitor of the central star decrease by $0.15\,M_\odot$.

The final, central star, mass for such a star is $0.66\,M_\odot$. However, we have shown that such a star would show a high C/O ≈ 2, whereas the presence of silicate features in the Spitzer spectrum indicate that C/O ≲ 1. To reconcile the mass and the abundances, we conjecture that the evolution was interrupted by the binary interaction that formed the disk, when the core mass was $0.61\,M_\odot$. With such a mass, the evolutionary time to the current position on the Hertzsprung–Russell diagram is in better agreement with the age of the nebula. This mass is also in better agreement with that derived from the photoionization model $(0.58 \pm 0.03)\,M_\odot$.

Photoionization modelling

The stratified ionization and excitation structure of NGC 3132 is evident in Fig. 1, wherein the bright rim of ionized gas, as traced by [S III] and Brackett α (Brα) emission, lies nestled inside the peak H_2 emission. However, significant ionized hydrogen and high-excitation plasma—traced by [Ne II] and [S III] emission in the MIRI F1280W and F1800W filter images, respectively—is observed beyond the bright inner, elliptical ring.

We constructed a 3D photoionization model using the code Mocassin[73]. To constrain the model, we used the Multi Unit Spectroscopic Explorer (MUSE) emission line maps and absolute Hβ flux of ref. [74], the optical integrated line fluxes from ref. [75], the IR line fluxes from ref. [76], as well as the velocity–position data obtained from the high-resolution scanning Fabry–Perot interferometer mounted on the Southern Astrophysics Research (SOAR) telescope adaptive module (SOAR Adaptive Optics Fabri–Perot [SAM-FP] instrument). The observations were taken

under photometric conditions. The seeing during the observations was 0.7 arcsec for the [N II] observations to 0.9 arcsec for the Hα one. The FWHM of Ne calibration lamp lines was 0.586 Å or 26.8 km s^{-1}, which corresponds to a spectral resolution of about 11,200 at Hα.

We determined the density structure by fitting the emission line maps to the SAM-FP images of [N II] λ6,584 and Hα, using a distance of 754 kpc. The model adopts as free parameters the temperature and luminosity of the ionizing source, and the elemental abundance of the gas component (assumed constant throughout the nebula); we assumed that no dust is mixed in the gas. For the ionizing source, we use the non-local thermodynamic equilibrium model atmospheres of central stars of planetary nebulae from ref. [77].

We find that a model invoking an unobscured central star with effective temperature $T_{\rm eff}$ = 110 kK and luminosity L = 200 $L_{\odot}$ well matches the observational data. However, we find that the present-day central star mass implied by the comparison between these stellar parameters and the evolutionary tracks of ref. [40] (0.58 ± 0.03 $M_{\odot}$) is inconsistent with the (large) initial mass inferred from consideration of the presence of the comoving, wide-separation A-type companion (0.66 $M_{\odot}$; see 'Central star system's masses'). Furthermore, the tracks of ref. [40] indicate that, for this mass, we would have a post-AGB age of 20,000 yr, whereas the position–velocity data from the SAM-FP instrument yield an expansion velocity of 25–35 km s^{-1}, implying a much shorter and inconsistent nebular dynamical age in the range 2,200–5,700 yr.

The C/O and N/O abundances of the nebula, as well as the crystalline silicate nature of the dust in the PN, indicate that this object has not undergone hot-bottom burning and that it has not undergone sufficient dredge up to have increased the C/O ratio above unity. By the time the 2.86 $M_{\odot}$ star reaches the tip of the AGB, its C/O ratio is approximately 2. It therefore seems that the mass implied by the initial-to-final mass relation using a main-sequence mass of 2.86 $M_{\odot}$ is too high. We have two ways to resolve this inconsistency (which may both be operating). The central star is shielded by dust in the circumstellar disk making it appear, to the PN, as a cooler star, and/or the central star mass is actually smaller than 0.66 $M_{\odot}$, because the AGB evolution was interrupted by a binary interaction.

If the stellar ascent of the AGB was interrupted, we can determine the upper limit for a mass that would produce a nebula with C/O $\lesssim$ 1 and N/O ≈ 0.4. This is 0.61 $M_{\odot}$. The time for a star of this mass to move from the AGB to the location on the Hertzsprung–Russell diagram with an approximate temperature and luminosity (110 kK and 200 $L_{\odot}$) as measured above is ~10,000 yr. The timescale of the transition from AGB to post-AGB and PN is tightly connected with the rate at which the envelope is consumed: the results obtained are therefore sensitive to the mass-loss description. The time of 10,000 yr, is based on the classic mass-loss rates dictated by Reimers or Blocker[78]. This estimate must be considered as an upper limit of the duration of this phase; indeed the recent works on the AGB to post-AGB transition by refs. [79,80] showed that to reproduce the IR excess of post-AGB stars in the Galaxy and in the Magellanic Clouds one has to invoke significantly higher mass-loss rates than those based on the aforementioned formulations, something that would reduce the timescales by a factor of about five. The timescale of 10,000 yr is therefore easily reconciled with the observed timescale of 2,200–5,700 yr implied by the nebula.

Hydrodynamic modelling

The hydrodynamic simulation used to interpret the fragmentation and radial spikes is a 2D hydrodynamic simulation using the magneto-hydrodynamic code ZEUS-3D. The computational grid is in spherical coordinates and consists of 800 × 800 equidistant zones in r and θ, respectively, with an angular extent of 90°. The wind and ultraviolet luminosity inputs correspond to a stellar post-AGB model with 0.677 $M_{\odot}$, which evolves from an initial 2.5 $M_{\odot}$ main-sequence star[81].

At simulation time 0 yr, the star has $T_{\rm eff}$ = 10,000 K and the AGB wind (v = 10 km s^{-1}, $\dot{M} = 10^{-6}$ $M_{\odot}$ yr^{-1}) has a homogeneous distribution outside of the pre-PN. The pre-PN has had 1,000 yr of evolution before this moment, during which time a wide magnetic jet operated with a velocity v = 230 km s^{-1}, and a mass-loss rate $\dot{M} = 1.3 \times 10^{-7}$ $M_{\odot}$ yr^{-1}; this simulation is taken from model C6 in ref. [82]. At this time, the star starts emitting a fast tenuous wind with a velocity v from 240 km s^{-1} to 14,000 km s^{-1} and a mass-loss rate $\dot{M}$ ranging from 1.06×10^{-7} $M_{\odot}$ yr^{-1} to 1.13×10^{-10} $M_{\odot}$ yr^{-1} over 4,000 yr that sweeps up the AGB wind material. At the same time (0 yr), the ionization front propagates into the medium.

Data availability

HST data are available at HST Legacy Archive (https://hla.stsci.edu). JWST data were obtained from the Mikulski Archive for Space Telescopes at the Space Telescope Science Institute (https://archive.stsci.edu/). MUSE data were collected at the European Organisation for Astronomical Research in the Southern Hemisphere, Chile (ESO Programme 60.A-9100), presented in ref. [74], and are available at the ESO Archive (http://archive.eso.org). San Pedro de Martir data are available at http://kincatpn.astrosen.unam.mx.

Code availability

The code MOCASSIN is available at https://mocassin.nebulousresearch.org/. ZEUS3-D is available at the Laboratory for Computational Astrophysics[84]). The compiled version of Shape is available at http://www.astrosen.unam.mx/shape.

References

1. Mastrodemos, N. & Morris, M. Bipolar pre-planetary nebulae: hydrodynamics of dusty winds in binary systems. II. Morphology of the circumstellar envelopes. *Astrophys. J.* **523**, 357–380 (1999).
2. Mohamed, S. & Podsiadlowski, P. Mass transfer in mira-type binaries. *Baltic Astron.* **21**, 88–96 (2012).
3. Maercker, M. et al. Unexpectedly large mass loss during the thermal pulse cycle of the red giant star R Sculptoris. *Nature* **490**, 232–234 (2012).
4. Santander-García, M. et al. ALMA high spatial resolution observations of the dense molecular region of NGC 6302. *Astron. Astrophys.* **597**, A27 (2017).
5. Sahai, R. & Trauger, J. T. Multipolar bubbles and jets in low-excitation planetary nebulae: toward a new understanding of the formation and shaping of planetary nebulae. *Astron. J.* **116**, 1357–1366 (1998).
6. Sahai, R., Morris, M. R. & Villar, G. G. Young planetary nebulae: Hubble Space Telescope imaging and a new morphological classification system. *Astron. J.* **141**, 134 (2011).
7. van Winckel, H. Post-AGB stars. *Annu. Rev. Astron. Astrophys.* **41**, 391–427 (2003).
8. Ivanova, N. et al. Common envelope evolution: where we stand and how we can move forward. *Astron. Astrophys. Rev.* **21**, 59 (2013).
9. Mastrodemos, N. & Morris, M. Bipolar preplanetary nebulae: hydrodynamics of dusty winds in binary systems. I. Formation of accretion disks. *Astrophys. J.* **497**, 303 (1998).
10. Mohamed, S. & Podsiadlowski, P. R. Wind Roche-lobe overflow: a new mass-transfer mode for wide binaries. In *15th European Workshop on White Dwarfs: Astronomical Society of the Pacific Conference Series Vol. 372* (eds. Napiwotzki, R. & Burleigh, M. R.) 397–400 (ASP, 2007).
11. de Val-Borro, M., Karovska, M. & Sasselov, D. Numerical simulations of wind accretion in symbiotic binaries. *Astrophys. J.* **700**, 1148–1160 (2009).
12. Soker, N. Visual wide binaries and the structure of planetary nebulae. *Astron. J.* **118**, 2424–2429 (1999).

13. Balick, B. et al. FLIERs and other microstructures in planetary nebulae. IV. Images of elliptical PNs from the Hubble Space Telescope. *Astron. J.* **116**, 360–371 (1998).
14. Sahai, R. & Trauger, J. T. Multipolar bubbles and jets in low-excitation planetary nebulae: toward a new understanding of the formation and shaping of planetary nebulae. *Astron. J.* **116**, 1357–1366 (1998).
15. Sabbadin, F., Turatto, M., Ragazzoni, R., Cappellaro, E. & Benetti, S. The structure of planetary nebulae: theory vs. practice. *Astron. Astrophys.* **451**, 937–949 (2006).
16. Steffen, W. & López, J. A. Morpho-kinematic modeling of gaseous nebulae with SHAPE. *Rev. Mexicana Astron. Astrofis.* **42**, 99–105 (2006).
17. Balick, B. & Frank, A. Shapes and shaping of planetary nebulae. *Annu. Rev. Astron. Astrophys.* **40**, 439–486 (2002).
18. De Marco, O. The origin and shaping of planetary nebulae: putting the binary hypothesis to the test. *Publ. Astron. Soc. Pac.* **121**, 316 (2009).
19. Jones, D. & Boffin, H. M. J. Binary stars as the key to understanding planetary nebulae. *Nat. Astron.* **1**, 0117 (2017).
20. Sahai, R., Wootten, A. & Clegg, R. E. S. CO in the bipolar planetary nebula NGC 3132. *Astron. Astrophys.* **234**, L1–L4 (1990).
21. Kastner, J. H., Weintraub, D. A., Gatley, I., Merrill, K. M. & Probst, R. G. H_2 emission from planetary nebulae: signpost of bipolar structure. *Astrophys. J.* **462**, 777 (1996).
22. Abramovici, A. et al. LIGO: the Laser Interferometer Gravitational-Wave Observatory. *Science* **256**, 325–333 (1992).
23. Amaro-Seoane, P. et al. Laser interferometer space antenna. Preprint at https://arxiv.org/abs/1702.00786 (2017).
24. Ivezic, Z. et al. Large Synoptic Survey Telescope: from science drivers to reference design. *Serbian Astron. J.* **176**, 1–13 (2008).
25. Santander-García, M. et al. The double-degenerate, super-Chandrasekhar nucleus of the planetary nebula Henize 2-428. *Nature* **519**, 63–65 (2015).
26. Chiotellis, A., Boumis, P. & Spetsieri, Z. T. The interaction of type Ia supernovae with planetary nebulae: the case of Kepler's supernova remnant. *Galaxies* **8**, 38 (2020).
27. Cikota, A., Patat, F., Cikota, S., Spyromilio, J. & Rau, G. Common continuum polarization properties: a possible link between proto-planetary nebulae and type Ia supernova progenitors. *Mon. Not. R. Astron. Soc.* **471**, 2111–2116 (2017).
28. Hora, J. L. et al. Infrared Array Camera (IRAC) observations of planetary nebulae. *Astrophys. J. Suppl. Ser.* **154**, 296–301 (2004).
29. Fang, X. et al. Extended structures of planetary nebulae detected in H_2 emission. *Astrophys. J.* **859**, 92 (2018).
30. Ramos-Larios, G. et al. Rings and arcs around evolved stars—I. Fingerprints of the last gasps in the formation process of planetary nebulae. *Mon. Not. R. Astron. Soc.* **462**, 610–635 (2016).
31. Guerrero, M. A., Ramos-Larios, G., Toalá, J. A., Balick, B. & Sabin, L. Rings and arcs around evolved stars—II. The carbon star AFGL 3068 and the planetary nebulae NGC 6543, NGC 7009, and NGC 7027. *Mon. Not. R. Astron. Soc.* **495**, 2234–2246 (2020).
32. Kim, H., Liu, S.-Y. & Taam, R. E. Templates of binary-induced spiral-shell patterns around mass-losing post-main-sequence stars. *Astrophys. J. Suppl. Ser.* **243**, 35 (2019).
33. Maes, S. et al. SPH modelling of companion-perturbed AGB outflows including a new morphology classification scheme. *Astron. Astrophys.* **653**, A25 (2021).
34. Aydi, E. & Mohamed, S. 3D models of the circumstellar environments of evolved stars: formation of multiple spiral structures. *Mon. Not. R. Astron. Soc.* **513**, 4405–4430 (2022).
35. Decin, L. et al. (Sub)stellar companions shape the winds of evolved stars. *Science* **369**, 1497–1500 (2020).
36. Méndez, R. H. A-type central stars of planetary nebulae—II. The central stars of NGC 2346, He 2-36 and NGC 3132. *Mon. Not. R. Astron. Soc.* **185**, 647–660 (1978).
37. Wright, E. L. et al. The Wide-field Infrared Survey Explorer (WISE): mission description and initial on-orbit performance. *Astron. J.* **140**, 1868–1881 (2010).
38. Su, K. Y. L. et al. A debris disk around the central star of the helix nebula? *Astrophys. J. Lett.* **657**, L41–L45 (2007).
39. Clayton, G. C. et al. Dusty disks around central stars of planetary nebulae. *Astron. J.* **147**, 142 (2014).
40. Ventura, P., Karakas, A., Dell'Agli, F., García-Hernández, D. A. & Guzman-Ramirez, L. Gas and dust from solar metallicity AGB stars. *Mon. Not. R. Astron. Soc.* **475**, 2282–2305 (2018).
41. Huang, S.-S. Modes of mass ejection by binary stars and the effect on their orbital periods. *Astrophys. J.* **138**, 471 (1963).
42. Soberman, G. E., Phinney, E. S. & van den Heuvel, E. P. J. Stability criteria for mass transfer in binary stellar evolution. *Astron. Astrophys.* **327**, 620–635 (1997).
43. van Winckel, H. et al. Post-AGB stars with hot circumstellar dust: binarity of the low-amplitude pulsators. *Astron. Astrophys.* **505**, 1221–1232 (2009).
44. Sahai, R. The starfish twins: two young planetary nebulae with extreme multipolar morphology. *Astrophys. J. Lett.* **537**, L43–L47 (2000).
45. Akashi, M. & Soker, N. Shaping "ears" in planetary nebulae by early jets. *Astrophys. J.* **913**, 91 (2021).
46. Bear, E. & Soker, N. Planetary nebulae that cannot be explained by binary systems. *Astrophys. J. Lett.* **837**, L10 (2017).
47. Hamers, A. S., Glanz, H. & Neunteufel, P. A statistical view of the stable and unstable roche lobe overflow of a tertiary star onto the inner binary in triple systems. *Astrophys. J. Suppl. Ser.* **259**, 25 (2022).
48. Glanz, H. & Perets, H. B. Simulations of common envelope evolution in triple systems: circumstellar case. *Mon. Not. R. Astron. Soc.* **500**, 1921–1932 (2021).
49. Höfner, S. & Olofsson, H. Mass loss of stars on the asymptotic giant branch. Mechanisms, models and measurements. *Astron. Astrophys. Rev.* **26**, 1 (2018).
50. Balick, B. et al. The illumination and growth of CRL 2688: an analysis of new and archival Hubble Space Telescope observations. *Astrophys. J.* **745**, 188 (2012).
51. Feigelson, E. D., Lawson, W. A. & Garmire, G. P. The ϵ Chamaeleontis young stellar group and the characterization of sparse stellar clusters. *Astrophys. J.* **599**, 1207–1222 (2003).
52. Duchêne, G. & Kraus, A. Stellar multiplicity. *Annu. Rev. Astron. Astrophys.* **51**, 269–310 (2013).
53. Monreal-Ibero, A. & Walsh, J. R. The MUSE view of the planetary nebula NGC 3132. *Astron. Astrophys.* **634**, A47 (2020).
54. Storey, J. W. V. Molecular hydrogen observations of southern planetary nebulae. *Mon. Not. R. Astron. Soc.* **206**, 521–527 (1984).
55. Kohoutek, L. & Laustsen, S. Central star of NGC 3132: a visual binary. *Astron. Astrophys.* **61**, 761–763 (1977).
56. Ciardullo, R., Jacoby, G. H., Ford, H. C. & Neill, J. D. Planetary nebulae as standard candles. II—The calibration in M31 and its companions. *Astrophys. J.* **339**, 53–69 (1989).
57. Meatheringham, S. J., Wood, P. R. & Faulkner, D. J. A study of some southern planetary nebulae. *Astrophys. J.* **334**, 862–874 (1988).
58. Bailer-Jones, C. A. L., Rybizki, J., Fouesneau, M., Demleitner, M. & Andrae, R. Estimating distances from parallaxes. V. Geometric and photogeometric distances to 1.47 billion stars in Gaia Early Data Release 3. *Astron. J.* **161**, 147 (2021).
59. O'Dell, C. R., McCullough, P. R. & Meixner, M. Unraveling the Helix nebula: its structure and knots. *Astron. J.* **128**, 2339–2356 (2004).

60. Meixner, M., McCullough, P., Hartman, J., Son, M. & Speck, A. The multitude of molecular hydrogen knots in the Helix nebula. *Astron. J.* **130**, 1784–1794 (2005).
61. Matsuura, M. et al. VLT/near-infrared integral field spectrometer observations of molecular hydrogen lines in the knots of the planetary nebula NGC 7293 (the Helix nebula). *Mon. Not. R. Astron. Soc.* **382**, 1447–1459 (2007).
62. Matsuura, M. et al. A "firework" of H_2 knots in the planetary nebula NGC 7293 (the Helix nebula). *Astrophys. J.* **700**, 1067–1077 (2009).
63. Kastner, J. H., Gatley, I., Merrill, K. M., Probst, R. & Weintraub, D. The bipolar symmetry of ring-like planetary nebulae: molecular hydrogen emission from halos. *Astrophys. J.* **421**, 600 (1994).
64. Manchado, A. et al. High-resolution imaging of NGC 2346 with GSAOI/GeMS: disentangling the planetary nebula molecular structure to understand its origin and evolution. *Astrophys. J.* **808**, 115 (2015).
65. Fang, X. et al. Extended structures of planetary nebulae detected in H_2 emission. *Astrophys. J.* **859**, 92 (2018).
66. Cardelli, J. A., Clayton, G. C. & Mathis, J. S. The relationship between infrared, optical, and ultraviolet extinction. *Astrophys. J.* **345**, 245 (1989).
67. Bohlin, R. C., Savage, B. D. & Drake, J. F. A survey of interstellar H I from L-alpha absorption measurements. II. *Astrophys. J.* **224**, 132 (1978).
68. Andriantsaralaza, M., Zijlstra, A. & Avison, A. CO in the C1 globule of the Helix nebula with ALMA. *Mon. Not. R. Astron. Soc.* **491**, 758–772 (2020).
69. Bourlot, J. L., Forêts, G. P. D. & Flower, D. R. The cooling of astrophysical media by H_2. *Mon. Not. R. Astron. Soc.* **305**, 802–810 (1999).
70. Wolniewicz, L., Simbotin, I. & Dalgarno, A. Quadrupole transition probabilities for the excited rovibrational states of H_2. *Astrophys. J. Suppl. Ser.* **115**, 293–313 (1998).
71. Marigo, P. et al. A new generation of PARSEC-COLIBRI stellar isochrones including the TP-AGB phase. *Astrophys. J.* **835**, 77 (2017).
72. Dotter, A. et al. The Dartmouth Stellar Evolution Database. *Astrophys. J. Suppl. Ser.* **178**, 89–101 (2008).
73. Ercolano, B., Barlow, M. J., Storey, P. J. & Liu, X. W. Mocassin: a fully three-dimensional Monte Carlo photoionization code. *Mon. Not. R. Astron. Soc.* **340**, 1136–1152 (2003).
74. Monreal-Ibero, A. & Walsh, J. R. The MUSE view of the planetary nebula NGC 3132. *Astron. Astrophys.* **634**, A47 (2020).
75. Tsamis, Y. G., Barlow, M. J., Liu, X.-W., Storey, P. J. & Danziger, I. J. A deep survey of heavy element lines in planetary nebulae—II. Recombination-line abundances and evidence for cold plasma. *Mon. Not. R. Astron. Soc.* **353**, 953–979 (2004).
76. Mata, H. et al. Spitzer mid-infrared spectroscopic observations of planetary nebulae. *Mon. Not. R. Astron. Soc.* **459**, 841–853 (2016).
77. Rauch, T. NLTE spectral analysis of the sdOB primary of the eclipsing binary system LB 3459 (AA Dor). *Astron. Astrophys.* **356**, 665–675 (2000).
78. Blöcker, T. Stellar evolution of low- and intermediate-mass stars. II. Post-AGB evolution. *Astron. Astrophys.* **299**, 755 (1995).
79. Kamath, D. et al. New Post-AGB star models as tools to understand AGB evolution and nucleosynthesis. Preprint at https://arxiv.org/abs/2112.05535 (2021).
80. Tosi, S. et al. Understanding dust production and mass loss on the AGB phase using post-AGB stars in the Magellanic Clouds. Preprint at https://arxiv.org/abs/2208.08314 (2022).
81. Villaver, E., Manchado, A. & García-Segura, G. The dynamical evolution of the circumstellar gas around low- and intermediate-mass stars. II. The planetary nebula formation. *Astrophys. J.* **581**, 1204–1224 (2002).
82. García-Segura, G., Taam, R. E. & Ricker, P. M. Common envelope shaping of planetary nebulae. III. The launching of jets in proto-planetary nebulae. *Astrophys. J.* **914**, 111 (2021).
83. Bradley, L. et al. astropy/photutils: 1.5.0. *Zenodo* https://doi.org/10.5281/zenodo.596036 (2022).
84. Clarke, D. A. A consistent method of characteristics for multidimensional magnetohydrodynamics. *Astrophys. J.* **457**, 291 (1996).

Acknowledgements

We acknowledge the International Astronomical Union that oversees the work of Commission H3 on Planetary Nebulae. It is through the coordinating activity of this committee that this paper came together. S.A. acknowledges support under the grant 5077 financed by IAASARS/NOA. J.A. and V.B. acknowledge support from the EVENTs/Nebulae-Web research programme, Spanish AEI grant PID2019-105203GB-C21. I.A. acknowledges the support of CAPES, Brazil (Finance Code 001). E.D.B. acknowledges financial support from the Swedish National Space Agency. E.G.B. acknowledges NSF grants AST-1813298 and PHY-2020249. J.C. and E.P. acknowledge support from an NSERC Discovery Grant. G.G.-S. thanks M. L. Norman and the Laboratory for Computational Astrophysics for the use of ZEUS-3D. D.A.G.-H. and A.M. acknowledge support from the ACIISI, Gobierno de Canarias and the European Regional Development Fund (ERDF) under grant with reference PROID2020010051 as well as from the State Research Agency (AEI) of the Spanish Ministry of Science and Innovation (MICINN) under grant PID2020-115758GB-I00. J.G.-R. acknowledges support from Spanish AEI under Severo Ochoa Centres of Excellence Programme 2020-2023 (CEX2019-000920-S). J.G.-R. and V.G.-L. acknowledge support from ACIISI and ERDF under grant ProID2021010074. D.R.G. acknowledges the CNPq grant 313016/2020-8. M.A.G. acknowledges support of grant PGC2018-102184-B-I00 of the Ministerio de Educación, Innovación y Universidades cofunded with FEDER funds and from the State Agency for Research of the Spanish MCIU through the 'Center of Excellence Severo Ochoa' award to the Instituto de Astrofísica de Andalucía (SEV-2017-0709). D.J. acknowledges support from the Erasmus+ programme of the European Union under grant number 2020-1-CZ01-KA203-078200. A.I.K. and Z.O. were supported by the Australian Research Council Centre of Excellence for All Sky Astrophysics in 3 Dimensions (ASTRO 3D), through project number CE170100013. This research is/was supported by an Australian Government Research Training Program (RTP) Scholarship. M.M. and R.W. acknowledge support from STFC Consolidated grant (2422911). C.M. acknowledges support from UNAM/DGAPA/PAPIIT under grant IN101220. S.S.M. acknowledges funding from UMiami, the South African National Research Foundation and the University of Cape Town VC2030 Future Leaders Award. J.N. acknowledges support from NSF grant AST-2009713. C.M.d.O. acknowledges funding from FAPESP through projects 2017/50277-0, 2019/11910-4 e 2019/26492-3 and CNPq, process number 309209/2019-6. J.H.K. and P.M.B. acknowledge support from NSF grant AST-2206033 and a NRAO Student Observing Support grant to Rochester Institute of Technology. M.O. was supported by JSPS Grants-in-Aid for Scientific Research(C) (JP19K03914 and 22K03675). Q.A.P. acknowledges support from the HKSAR Research grants council. Vera C. Rubin Observatory is a Federal project jointly funded by the National Science Foundation (NSF) and the Department of Energy (DOE) Office of Science, with early construction funding received from private donations through the LSST Corporation. The NSF-funded LSST (now Rubin Observatory) Project Office for construction was established as an operating centre under the management of the Association of Universities for Research in Astronomy (AURA). The DOE-funded effort to build the Rubin Observatory LSST Camera (LSSTCam) is managed by SLAC National Accelerator Laboratory (SLAC). A.J.R. was supported by the

Australian Research Council through award number FT170100243. L.S. acknowledges support from PAPIIT UNAM grant IN110122. C.S.C.'s work is part of I+D+i project PID2019-105203GB-C22 funded by the Spanish MCIN/AEI/10.13039/501100011033. M.S.-G. acknowledges support by the Spanish Ministry of Science and Innovation (MICINN) through projects AxIN (grant AYA2016-78994-P) and EVENTs/Nebulae-Web (grant PID2019-105203GB-C21). R.S.'s contribution to the research described here was carried out at the Jet Propulsion Laboratory, California Institute of Technology, under a contract with NASA. J.A.T. thanks the Marcos Moshisnky Fundation (Mexico) and UNAM PAPIIT project IA101622. E.V. acknowledges support from the 'On the rocks II project' funded by the Spanish Ministerio de Ciencia, Innovación y Universidades under grant PGC2018-101950-B-I00. A.A.Z. acknowledges support from STFC under grant ST/T000414/1. This research made use of Photutils, an Astropy package for detection and photometry of astronomical sources[83], of the Spanish Virtual Observatory (https://svo.cab.inta-csic.es) project funded by MCIN/AEI/10.13039/501100011033/ through grant PID2020-112949GB-I00 and of the computing facilities available at the Laboratory of Computational Astrophysics of the Universidade Federal de Itajubá (LAC-UNIFEI, which is maintained with grants from CAPES, CNPq and FAPEMIG). Based on observations made with the NASA/ESA Hubble Space Telescope, and obtained from the Hubble Legacy Archive, which is a collaboration between the Space Telescope Science Institute (STScI/NASA), the Space Telescope European Coordinating Facility (ST-ECF/ESAC/ESA) and the Canadian Astronomy Data Centre (CADC/NRC/CSA). The JWST Early Release Observations and associated materials were developed, executed and compiled by the ERO production team: H. Braun, C. Blome, M. Brown, M. Carruthers, D. Coe, J. DePasquale, N. Espinoza, M. Garcia Marin, K.Gordon, A. Henry, L. Hustak, A. James, A. Jenkins, A. Koekemoer, S. LaMassa, D. Law, A. Lockwood, A. Moro-Martin, S. Mullally, A. Pagan, D. Player, K. Pontoppidan, C. Proffitt, C. Pulliam, L. Ramsay, S. Ravindranath, N. Reid, M. Robberto, E. Sabbi, L. Ubeda. The EROs were also made possible by the foundational efforts and support from the JWST instruments, STScI planning and scheduling, and Data Management teams. Finally, this work would not have been possible without the collaborative platforms Slack (slack.com) and Overleaf (overleaf.com).

Author contributions

The following authors have contributed majorly to multiple aspects of the work that lead to this paper, the writing and the formatting of figures: O.D. (writing, structure, interpretation and synthesis), I.A. (H_2 interpretation), B.B. (processing and interpreting images), G.G.-S. (2D hydro modelling), J.H.K. (writing, H_2 measurements and interpretation), M.M. (imaging, photometry and H_2 interpretation), B.M. (stellar photometry), S.S.M. (hydrodynamics of binaries), A.M.-I. (MUSE data analysis), H.M. (photoionization and morpho-kinematic models), P.M.B. (JWST image production), C.M. (photoionization modelling), R.S. (disk model and comparative interpretation), N.S. (hydro modelling and interpretation), L. Stanghellini (distances and abundance interpretation), W.S. (morpho-kinematic models), J.R.W. (spatially resolved spectroscopy), A.A.Z. (disk model, H_2 measurements, writing and interpretation). The following authors have contributed key expertise to aspects of this paper: M.A. (hydrodynamic modelling and jet interpretation), J.A. (CO observations), S.A. (H_2 interpretation), P.A. (space-resolved spectroscopy), E.G.B. (hydrodynamics), J.B. (HST and radio images of fast evolving PN), B. Bucciarelli (Gaia data), V.B. (radio observations, disk observation and interpretation, and comparative studies), Y.-H.C. (disk interpretation), J.C. (molecular formation), R.L.M.C. (final review and interpretation), D.A.G.-H. (IR dust/PAH features and abundances), J.G.-R. (photoionization modelling), V.G.-L. (photoionization modelling), D.R.G. (comparative analysis), M.A.G. (X-ray imaging), D.J. (close binaries), A.I.K. (final review and stellar nucleosynthesis), A.M. (nebular morphology and H_2 interpretation), I.M. (photometry modelling), R.M. (X-ray and ultraviolet imaging), Z.O. (binary nucleosynthesis), M.O. (IR imaging), Q.A.P. (morphology), E.P. (nebular spectroscopy and PAHs), A.J.R. (binary populations), L. Sabin (abundances), C.S.C. (radio), M.S.-G. (nebular evolution), I.S. (star and star nebula association), A.K.S. (dust), J.A.T. (morphology), T.U. (nebular imaging), G.V.d.S. (IR observations), P.V. (AGB evolution model). The following authors contributed by commenting on some aspects of the analysis and manuscript: E.D.B., H.M.J.B., P.B., N.C., A.F., S.K., F.L., J.N., C.M.d.O., B.C.Q., G.Q.-L., M.R., E.V., W.V., R.W. and H.V.W.

Competing interests

The authors declare no competing interests.

Additional information

Supplementary information The online version contains supplementary material available at https://doi.org/10.1038/s41550-022-01845-2.

Correspondence and requests for materials should be addressed to Orsola De Marco.

Peer review information *Nature Astronomy* thanks Eric Lagadec and the other, anonymous, reviewer(s) for their contribution to the peer review of this work.

Reprints and permissions information is available at www.nature.com/reprints.

Publisher's note Springer Nature remains neutral with regard to jurisdictional claims in published maps and institutional affiliations.

Orsola De Marco[1,2] ✉, Muhammad Akashi[3,4], Stavros Akras[5], Javier Alcolea[6], Isabel Aleman[7], Philippe Amram[8], Bruce Balick[9], Elvire De Beck[10], Eric G. Blackman[11,12], Henri M. J. Boffin[13], Panos Boumis[5], Jesse Bublitz[14], Beatrice Bucciarelli[15], Valentin Bujarrabal[6], Jan Cami[16,17,18], Nicholas Chornay[19], You-Hua Chu[20], Romano L. M. Corradi[21,22], Adam Frank[11], D. A. García-Hernández[22,23], Jorge García-Rojas[22,23], Guillermo García-Segura[24], Veronica Gómez-Llanos[22,23], Denise R. Gonçalves[25], Martín A. Guerrero[26], David Jones[22,23], Amanda I. Karakas[27,28], Joel H. Kastner[29,30], Sun Kwok[31], Foteini Lykou[32,33], Arturo Manchado[22,23,34], Mikako Matsuura[35], Iain McDonald[36,37], Brent Miszalski[38], Shazrene S. Mohamed[39,40,41,42], Ana Monreal-Ibero[43], Hektor Monteiro[7], Rodolfo Montez Jr[44], Paula Moraga Baez[30], Christophe Morisset[24], Jason Nordhaus[45,46],

Claudia Mendes de Oliveira[47], Zara Osborn[27,28], Masaaki Otsuka[48], Quentin A. Parker[49,50], Els Peeters[16,17,18], Bruno C. Quint[51], Guillermo Quintana-Lacaci[52], Matt Redman[53], Ashley J. Ruiter[54], Laurence Sabin[24], Raghvendra Sahai[55], Carmen Sánchez Contreras[56], Miguel Santander-García[6], Ivo Seitenzahl[54], Noam Soker[3], Angela K. Speck[57], Letizia Stanghellini[58], Wolfgang Steffen[59], Jesús A. Toalá[60], Toshiya Ueta[61], Griet Van de Steene[62], Hans Van Winckel[63], Paolo Ventura[64], Eva Villaver[56], Wouter Vlemmings[65], Jeremy R. Walsh[13], Roger Wesson[35] & Albert A. Zijlstra[37]

[1]School of Mathematical and Physical Sciences, Macquarie University, Sydney, New South Wales, Australia. [2]Astronomy, Astrophysics and Astrophotonics Research Centre, Macquarie University, Sydney, New South Wales, Australia. [3]Department of Physics, Technion, Haifa, Israel. [4]Kinneret College on the Sea of Galilee, Samakh, Israel. [5]Institute for Astronomy, Astrophysics, Space Applications and Remote Sensing, National Observatory of Athens, Penteli, Greece. [6]Observatorio Astronómico Nacional (OAN/IGN), Madrid, Spain. [7]Instituto de Física e Química, Universidade Federal de Itajubá, Itajubá, Brazil. [8]Aix-Marseille Université, CNRS, CNES, LAM (Laboratoire d'Astrophysique de Marseille), Marseille, France. [9]Astronomy Department, University of Washington, Seattle, WA, USA. [10]Department of Space, Earth and Environment, Chalmers University of Technology, Gothenburg, Sweden. [11]Department of Physics and Astronomy, University of Rochester, Rochester, NY, USA. [12]Laboratory for Laser Energetics, University of Rochester, Rochester, NY, USA. [13]European Southern Observatory, Garching, Germany. [14]Green Bank Observatory, Green Bank, WV, USA. [15]INAF - Osservatorio Astrofisico di Torino, Pino Torinese, Italy. [16]Department of Physics and Astronomy, University of Western Ontario, London, Ontario, Canada. [17]Institute for Earth and Space Exploration, University of Western Ontario, London, Ontario, Canada. [18]SETI Institute, Mountain View, CA, USA. [19]Institute of Astronomy, University of Cambridge, Cambridge, UK. [20]Institute of Astronomy and Astrophysics, Academia Sinica (ASIAA), Taipei, Taiwan. [21]GRANTECAN, La Palma, Spain. [22]Instituto de Astrofísica de Canarias, La Laguna, Spain. [23]Departamento de Astrofísica, Universidad de La Laguna, La Laguna, Spain. [24]Instituto de Astronomía, Universidad Nacional Autónoma de México, Ensenada, Mexico. [25]Observatório do Valongo, Universidade Federal do Rio de Janeiro, Rio de Janeiro, Brazil. [26]Instituto de Astrofísica de Andalucía, IAA-CSIC, Glorieta de la Astronomía, Granada, Spain. [27]School of Physics and Astronomy, Monash University, Clayton, Victoria, Australia. [28]ARC Centre of Excellence for All Sky Astrophysics in 3 Dimensions (ASTRO 3D), Canberra, Australian Capital Territory, Australia. [29]Center for Imaging Science, Rochester Institute of Technology, Rochester, NY, USA. [30]School of Physics and Astronomy and Laboratory for Multiwavelength Astrophysics, Rochester Institute of Technology, Rochester, NY, USA. [31]Department of Earth, Ocean, and Atmospheric Sciences, University of British Columbia, Vancouver, British Columbia, Canada. [32]Konkoly Observatory, Research Centre for Astronomy and Earth Sciences, Eötvös Loránd Research Network (ELKH), Budapest, Hungary. [33]CSFK, MTA Centre of Excellence, Budapest, Hungary. [34]Consejo Superior de Investigaciones Científicas, Madrid, Spain. [35]School of Physics and Astronomy, Cardiff University, Cardiff, UK. [36]Department of Physical Sciences, The Open University, Milton Keynes, UK. [37]Jodrell Bank Centre for Astrophysics, Department of Physics and Astronomy, The University of Manchester, Manchester, UK. [38]Australian Astronomical Optics, Faculty of Science and Engineering, Macquarie University, North Ryde, New South Wales, Australia. [39]Department of Physics, University of Miami, Coral Gables, FL, USA. [40]South African Astronomical Observatory, Cape Town, South Africa. [41]Astronomy Department, University of Cape Town, Rondebosch, South Africa. [42]NITheCS National Institute for Theoretical and Computational Sciences, Stellenbosch, South Africa. [43]Leiden Observatory, Leiden University, Leiden, the Netherlands. [44]Center for Astrophysics, Harvard & Smithsonian, Cambridge, MA, USA. [45]Center for Computational Relativity and Gravitation, Rochester Institute of Technology, Rochester, NY, USA. [46]National Technical Institute for the Deaf, Rochester Institute of Technology, Rochester, NY, USA. [47]Departamento de Astronomia, Instituto de Astronomia, Geofísica e Ciências Atmosféricas da USP, Cidade Universitária, São Paulo, Brazil. [48]Okayama Observatory, Kyoto University, Asakuchi, Japan. [49]Department of Physics, The University of Hong Kong, Hong Kong SAR, China. [50]Laboratory for Space Research, Hong Kong SAR, China. [51]Rubin Observatory Project Office, Tucson, AZ, USA. [52]Department of Molecular Astrophysics, IFF-CSIC, Madrid, Spain. [53]Centre for Astronomy, School of Physics, National University of Ireland Galway, Galway, Ireland. [54]University of New South Wales, Australian Defence Force Academy, Canberra, Australian Capital Territory, Australia. [55]Jet Propulsion Laboratory, California Institute of Technology, Pasadena, CA, USA. [56]Centro de Astrobiología (CAB), CSIC-INTA, Madrid, Spain. [57]Department of Physics and Astronomy, Applied Engineering and Technology Building, University of Texas at San Antonio, San Antonio, TX, USA. [58]NSF's NOIRLab, Tucson, AZ, USA. [59]ilumbra, AstroPhysical MediaStudio, Kaiserslautern, Germany. [60]Instituto de Radioastronomía y Astrofísica, UNAM, Morelia, Mexico. [61]Department of Physics and Astronomy, University of Denver, Denver, CO, USA. [62]Royal Observatory of Belgium, Astronomy and Astrophysics, Brussels, Belgium. [63]Institute of Astronomy, KULeuven, Leuven, Belgium. [64]INAF – Osservatorio Astronomico di Roma, Rome, Italy. [65]Onsala Space Observatory, Department of Space, Earth and Environment, Chalmers University of Technology, Onsala, Sweden. ✉e-mail: orsola.demarco@mq.edu.au